RSC Applied Polymers

ROYAL SOCIETY OF CHEMISTRY

PAPER

View Article Online
View Journal | View Issue

Check for updates

Cite this: *RSC Appl. Polym.*, 2025, **3**, 1340

Hydrogel-filled tubular scaffolds for directional tissue regeneration combining shape-memory polyester blends with hyaluronic acid click-hydrogels†

Álvaro Hidalgo-Yerga,[a,b] Leonor Resina,[a,b] Jordi Casanovas,[c] Hamidreza Enshaei,[a,b] Francesc Estrany,[a,b] José I. Iribarren,[a,b] Maria M. Pérez-Madrigal *[a,b] and Carlos Alemán *[a,b,d]

A clinical need still exists for advanced therapeutics to improve the recovery of patients suffering from large-gap peripheral nerve injuries (PNI). In this study, tubular constructs of submicrometric thickness (<1 μm) are prepared using shape-memory 50 : 50, 70 : 30 and 90 : 10 poly(lactic acid) (PLA)/polycaprolactone (PCL) blends, which are filled with a hyaluronic acid (HA)-based hydrogel. The hydrogel is crosslinked *in situ* by click chemistry using a 3-arm alkyne-functionalized polyethylene glycol and thiol-modified HA. The Young's moduli of the hydrogels confined inside the different cylindrical constructs are similar to that of the free hydrogel, the tubular shell mainly affecting the tensile strength and deformability. On the other hand, cell adhesion and proliferation assays demonstrate that the cytocompatibility of the blends, the hydrogel and the filled tubular constructs is similar to or even higher than that of the tissue culture polystyrene used as the control. Furthermore, the scaffold derived from the 70 : 30 PLA/PCL blend provides a 3D cell-friendly mechanical environment that promotes the directional migration of cells towards the confined hydrogel. The engineered scaffolds may have important implications in the repairing of directional tissues.

Received 6th April 2025,
Accepted 24th July 2025

DOI: 10.1039/d5lp00098j

rsc.li/rscapplpolym

Introduction

In recent years, shape-memory polymers (SMPs), which are intelligent materials with the ability to actively change their shape under stimulus (*e.g.* thermal, magnetic, chemical, light, and electrical), have attracted significant attention in the biomedical field.[1–5] In particular, advances in tissue regeneration have promoted the investigation of biodegradable SMPs as smart scaffolds since their chemical and physical properties potently direct cell regeneration.[6–9] SMPs used for scaffold fabrication must not only provide the necessary mechanical support, but also offer unique and differentiating characteristics. For example, the shape-shifting feature of these materials allows them to faithfully fill tissue defects of varied and, sometimes, irregular geometries.[6]

On the other hand, peripheral nerve injuries (PNI), which can result in complete loss of motor/sensor functionalities, muscle paralysis, and neuropathic pain, affect annually hundreds of thousands of individuals as a consequence of acute trauma.[10–13] When damaged, peripheral nerves respond to the injury by activating intrinsic signaling pathways in an attempt to self-repair and promote outgrowing axons.[14] Unfortunately, large gaps (*i.e.*, larger than 2 cm) hinder this natural response, and surgical intervention is required to bridge the gap and aid regeneration. Current clinical gold standard therapies for large gap PNI, which include end-to-end suturing (for gaps lower than 1 cm), healthy autologous nerve grafting, and acellular or cellular allograft implantation (for 1–5 cm gaps), still do not adequately address this worldwide health problem. The use of donor sites displays several limitations, such as permanent donor site morbidity or functional loss, necrosis, and neurofibroma formation, while exhibiting decreased efficiency for gaps >5 cm. Furthermore, full restoration is rarely accomplished and, hence, a major clinical need still exists for

[a]*IMEM-BRT Group, Departament d'Enginyeria Química, EEBE, Universitat Politècnica de Catalunya, C/Eduard Maristany 10-14, Ed. I2, 08019 Barcelona, Spain. E-mail: m.mar.perez@upc.edu*
[b]*Barcelona Research Center for Multiscale Science and Engineering, Universitat Politècnica de Catalunya, C/Eduard Maristany 10-14, Ed. C, 08019 Barcelona, Spain. E-mail: carlos.aleman@upc.edu*
[c]*Departament de Química, Física i Ciències Ambientals i del Sòl, Escola Politècnica Superior, Universitat de Lleida, c/Jaume II no. 69, Lleida E-25001, Spain*
[d]*Institute for Bioengineering of Catalonia (IBEC), The Barcelona Institute of Science and Technology, Baldiri Reixac 10-12, 08028 Barcelona, Spain*
† Electronic supplementary information (ESI) available. See DOI: https://doi.org/10.1039/d5lp00098j

alternative therapeutics to improve the prognosis for patients suffering from PNI.[12] Indeed, despite the high incidence of PNI, their clinical relevance and the efforts undertaken, the therapeutic advances have not been much within the last 30 years.[12]

By applying tissue engineering and regenerative medicine approaches, biomaterial-based nerve guidance conduits (NGCs) are designed as tubular constructs, with a hollow or filled luminal space, to bridge injury sites and provide physical support for the regeneration of peripheral nerves.[15–17] The criteria for the choice of the materials to manufacture NGCs has evolved to include: (i) adequate mechanical features to support nerve regeneration; (ii) permeability to promote nutrient diffusion; and (iii) biodegradability, which eliminates the need for a subsequent surgery to remove the conduit, or the occurrence of nerve compression. As the starting part of a wide and long-term project devoted to nerve tissue regeneration, in this study, we present the construction and characterization of biocompatible filled tubular constructs using biodegradable self-standing microfilms of SMPs with a hyaluronic acid (HA)-based hydrogel for tissue regeneration.

On account of their biocompatibility and biodegradability, polylactic acid (PLA),[18–21] poly(ε-caprolactone) (PCL),[20–23] their copolymers[20,21,24,25] and mixtures (blends)[20,21,26,27] are frequently used as SMPs in biomedical applications. However, while NGCs based on neat PLA can be limited by the high degradation rate of such materials, which continuously reduces in the short term the initial excellent mechanical properties and releases acidic degradation products, the utilization of neat PCL is precluded by its high rigidity, which may lead to breakage and other complications after implantation. The SMPs of PLA/PCL blends are explained by the different thermomechanical properties of the two polymers, which are thermodynamically immiscible but compatible polymers. PLA acts as a reversible phase and provides stronger resilience than PCL. Thus, the amount of PCL promotes the shape fixing ability of the blends whereas the PLA content enhances the shape recovery capability.[20,21,26,27] In a recent work devoted to studying macroscopic tubular specimens (*i.e.*, 4 × 6 × 0.1 cm^3), we found that the shape memory and mechanical properties of PLA/PCL blends are not only suitable for nerve regeneration applications, but also easily tunable through their composition (*i.e.*, the PLA : PCL ratio in the mixture).[26]

Herein, we present the first model of a device that we hope to use in the near future for peripheral nerve regeneration. This first model is based on an HA-based hydrogel that has been confined inside hollow tubular constructs of submicrometric thickness. More specifically, tubular constructs have been initially prepared using PLA/PCL blends with different compositions. After evaluating their properties and suitability as NGCs, such hollow structures have been filled with the HA-based hydrogel, which has been crosslinked *in situ* by click chemistry.[28,29] The confined hydrogel, hereafter named clickHA, has been incorporated by infiltrating inside the microtube the HA modified with thiol moieties and the crosslinker, which is an alkyne-functionalized polyethylene glycol ($PEG_{3\text{-arm}}$). Finally, we demonstrate both the cytocompatibility of the filled tubular microconstruct and the ability of cells to migrate across the construct towards the confined hydrogel.

Methods

Materials

PLA 2002D, a product of Natureworks, was kindly supplied by Nupik International (Polinyà, Spain). According to the manufacturer, this PLA has a D content of 4.25%, a residual monomer content of 0.3%, and a density of 1.24 g cm^{-3}. PCL (beads) with a density of 1.15 g cm^{-3} was purchased from Sigma-Aldrich. For both polymers, Table S1† displays the glass transition and melting temperatures (T_g and T_m, respectively), as determined by differential scanning calorimetry (DSC), and the number average molecular weight (M_n), the weight average molecular weight (M_w) and the polydispersity index (PDI = M_w/M_n), as determined by gel permeation chromatography (GPC).

Poly(vinyl alcohol) (PVA) 87–89% hydrolyzed (M_w = 13 000–23 000 g mol^{-1}) was purchased from Sigma-Aldrich (USA). Acetone and chloroform were purchased from Panreac Quimica S.A.U. (Spain).

For the synthesis of the click-hydrogel, HA sodium salt (40–50 kDa; product code FH01773) was purchased from Carbosynth, while 3,3′-dithiobis(propanoic dihydrazide) (DTPHY, 99%; product code FT-FSID13817) was purchased from Frontier Scientific. The remaining reagents, which included 2-(*N*-morpholino)ethanesulfonic acid (MES low moisture content, >99% – M3671), *N*-ethyl-*N*′-(3-dimethylaminopropyl) carbodiimide hydrochloride (EDAC hydrochloride – product number 341006), tris(2-carboxyethyl)phosphine hydrochloride (TCEP·HCl, powder, ≥98%, C4706), glycerol ethoxylate (~1000 g mol^{-1} (n = 6–7)), propiolic acid (95%), potassium hydroxide (KOH; ≥85%), sodium hydroxide (NaOH; ≥97%), and sodium chloride (NaCl, ACS grade), were purchased from Sigma-Aldrich and used as received without further purification.

Self-standing microfilms of PLA/PCL

Given amounts of neat PLA and PCL were mixed considering three different PLA : PCL weight ratios (90 : 10, 70 : 30, and 50 : 50). In order to obtain 100 mg mL^{-1} (10 wt%) solutions, the PLA : PCL mixtures were dissolved in 2 : 1 chloroform : acetone. For the fabrication of films of submicrometric thickness, 2 mL of the corresponding solution mixture was spin-coated using a WS-400BZ-6NPP/A1/AR1 spin-coater (Laurell Technologies Corporation) for 30 s at an angular speed of 1400 rpm onto a stainless steel substrate (2.5 × 2.5 cm^2) previously coated with a PVA sacrificial layer. The PVA layer was obtained by spin-coating at 2100 rpm for 2 min 600 μL of a PVA solution in Milli-Q® water (100 mg mL^{-1}) onto the stainless steel substrate. Once prepared, the steel-supported membranes were left to dry and cut with a cutter into three equal membranes of 0.83 × 2.5 cm^2. Next, samples were immersed overnight in Milli-Q® water for the separation of the three microfilms from

the substrate by dissolving the PVA sacrificial layer. Finally, detached self-standing films were allowed to dry on a Teflon® surface to prevent them from sticking together.

PLA/PCL tubular constructs

The thermoresponsive shape memory characteristics of the PLA/PCL blends were used to form the tubes. The self-standing microfilms were subjected to the following three-step treatment. First, the self-standing PLA/PCL microfilm was immersed in water at 60 °C for 1 min. Once this time passed, the membrane was rolled along a 2 mm diameter PLA rod, obtained by 3D printing, with the help of tweezers so that it acquired the shape of a spiral (temporary state). Finally, to fix the temporary state, the microfilm was immersed (still on the PLA rod) in water at room temperature. When detached from the PLA with the help of tweezers, the formed tubes were carefully dried with absorbent paper.

Filling PLA/PCL constructs with the confined clickHA hydrogel

The PLA/PCL tubular constructs were filled with a click-hydrogel made of hyaluronic acid (clickHA) crosslinked with a modified polyethylene glycol precursor (PEG). For this purpose, HA was modified with thiol moieties (HA-SH) following an already reported procedure.[28] On the other hand, the synthesis of 3-arm alkyne-PEG ($PEG_{3\text{-arm}}$) was performed by esterifying glycerol ethoxylate with propiolic acid, as previously reported.[30] Details of the synthesis of HA-SH and $PEG_{3\text{-arm}}$ are provided in the ESI.†

ClickHA (HA-S-ene-PEG) hydrogels (clickHA) were confined inside the PLA/PCL microtubes by *in situ* gelation. For this purpose, 31.3 mg of HA-SH were dissolved in 300 μL of phosphate-buffered saline solution (PBS) by mild vortexing. Then, 3.5 mg of the $PEG_{3\text{-arm}}$ crosslinker, previously dissolved in 100 μL of PBS, were added to the HA-SH solution. After vigorous stirring (20–30 s), the pH of the HA-SH : $PEG_{3\text{-arm}}$ mixture was adjusted to ~7 (physiological pH) by injecting 20 μL of KOH 1 M. Immediately after adjusting the pH, the neutralized mixture was injected into the PLA/PCL microtubular construct using a syringe. Although gelation was fast (<60 s), the confined hydrogels were left to gel overnight at 4 °C.

Characterization

The AFM scratching technique was used to characterize the surface topography and phase distribution, as well as to measure the thickness of the PLA/PCL microfilms. Specifically, contact mode AFM was used to intentionally scratch microfilms deposited on the stainless steel substrate. A line profile determined across the scratch with tapping mode AFM was used to determine the film thickness from the depth of the scratch. It should be noted that the topographic image was taken of a region bigger than the scratch area so as to accurately measure the step between the coated and the uncoated surface. Images were obtained with an AFM Dimension 3100 microscope using a NanoScope IV controller. AFM was operated under ambient conditions at a scan speed of 0.8–1 Hz, in the tapping mode and using single-beam silicon cantilever probes with a nominal tip radius of 10 nm (TAP 150-G probes; Budget Sensors, Bulgaria).

In addition, the film thickness was also determined using a Dektak 150 stylus profilometer (Veeco, Plainview, NY). Imaging of the films was conducted using the following optimized settings: tip radius = 2.5 μm; stylus force = 3.0 mg; scan length = 1 μm; duration 30 seconds.

FTIR spectra were recorded using a Jasco© FTIR 4700 spectrometer equipped with an attenuated total reflection accessory (Top-plate) with a diamond crystal (Specac model MKII Golden Gate Heated Single Reflection Diamond ATR). Each spectrum was obtained using an average of 64 scans in the range of 600–4000 cm^{-1} with a resolution of 4 cm^{-1}.

Raman spectra were acquired using a Renishaw dispersive Raman microscope spectrometer (model InVia Qontor, GmbH, Germany) and Renishaw WiRE software. The spectrometer is equipped with a Leica DM2700 M optical microscope, a thermo-electrically cooled charge-coupled device (CCD) detector (−70 1C, 1024 × 256 pixels) and spectrograph scattered light with 2400 lines per mm or 1200 lines per mm of grating. The experiments were performed at a 785 nm excitation wavelength and with a nominal laser output power of 500 mW. The exposure time was 10 s, the laser power was adjusted to 100% of its nominal output power and each spectrum was recorded with four accumulations. All Raman spectra were recorded in a spectral range from 600 to 4000 cm^{-1} with the same measurement parameters.

X-ray diffraction (XRD) intensities of PLA/PCL films were collected using a Bruker D8 Advance diffractometer with a one-dimensional Lynx Eye detector and monochromated Cu-K_α radiation. The 2θ range was from 5° to 60°.

Water contact angle (WCA) measurements were carried out using the sessile drop method at room temperature. Images of Milli-Q water drops (2.6 μL) were recorded with a DSA25S (Krüss GmbH) after stabilization (10 s) and analyzed using the Advance (Krüss) software. For each sample, the average WCA value and the corresponding standard deviation were derived from ten independent measurements at least.

The mechanical properties of PLA/PCL films were evaluated with a universal testing machine (EZ-Test LX, Shimadzu) fitted with a load cell of 100 N under controlled laboratory conditions (22 °C and 40% relative humidity). For tensile testing, the deformation rate for stress–strain assays was 10 mm min^{-1}. Rectangular PLA/PCL films of dimensions 2.5 ± 0.1 and 0.8 ± 0.03 mm and a thickness of 1.0 ± 0.1 mm were prepared. The elastic modulus (E), the tensile strength (σ_{max}) and the elongation at break (ε_{break}) were obtained from ten independent measurements. After discarding the two experiments with greater divergence, average values (± standard deviation) were computed considering the remaining eight samples. On the other hand, the mechanical properties of clickHA hydrogels and of tubular constructs filled with the hydrogel were determined by uniaxial compressive testing using the same equipment. ClickHA hydrogel samples (n = 4) were prepared with a cylindrical shape (diameter of 9.0–9.5 mm and height of 7 mm on average) using the gelation conditions optimized

for its confinement inside the tubes (see above), while the diameter and height of filled cylindrical tubes (n = 4) were 2 mm and 2 cm, respectively. A preload force of 0.05 N was set, and each test was performed at a compression rate of 1 mm min^{-1}. Data were recorded and analyzed using TRAPEZIUM-X analysis software (version 1.5.7, Shimadzu Corporation).

Scanning electron microscopy (SEM) studies were performed using a Focus Ion Beam Zeiss Neon 40 instrument (Carl Zeiss, Germany). Samples were mounted on a double-sided adhesive carbon disc and sputter-coated with a thin layer of carbon to prevent sample charging problems. All micrographs were recorded at an accelerating voltage of 5 kV.

X-ray computed microtomography (μ-CT, Skyscan 1272 microtomography, Bruker, USA) was performed as follows. The measurements were carried out at 50 kV voltage and 200 μA current without a filter and the projected images were collected every 0.2° over 180° with an exposure time of 570 ms, obtaining an isotropic voxel size (voxel resolution) of 3.3 μm. The nRecon software (Bruker, USA) was used for the reconstruction of the samples by alignment adjustment, beam hardening correction and ring artefact filtering. The porosity analysis was carried out using the CTAn software (Bruker, USA). Specifically, the image was binary segmented, smoothed by eliminating white/black speckles less than 15 voxels and finally measured. Parallel to that, the CTvox software was used to render 3D reconstructions (Bruker, USA).

Differential scanning calorimetry (DSC) of filled tubular constructs was performed using a TA Instruments Q100 series (New Castle, DE, USA) with T_{zero} technology and equipped with a refrigerated cooling system (RCS, TA Instruments, New Castle, DE, USA). Thermograms were obtained from approximately 3 mg of solid samples. The crystallization and melting temperatures and enthalpies were obtained from the second heating scans recorded at heating and cooling rates of 10 °C min^{-1} in all cases. The standards used for temperature and enthalpy calibrations were indium. Thermal characterization studies were conducted applying the following protocol: a heating run from 20 to 200 °C, a cooling run to −20 °C after keeping the sample in the melt state for 1 min, and, after 1 min, a second heating run from −20 to 200 °C.

Thermogravimetric analysis (TGA) of hot-pressed films was performed under a nitrogen atmosphere with Q50 (TA Instruments) equipment at a heating rate of 20 °C min^{-1} (sample weight *ca.* 5 mg) in the range between 40 and 600 °C.

Theoretical calculations

The strength of PLA···PCL, PLA···HA and PCL···HA interactions was examined using Density Functional Theory (DFT) calculations, which were performed using the Gaussian 09 computer package.[31] The geometries of the different investigated model complexes were fully optimized with the B3LYP[32–34] functional combined with the 6-311++G(d,p) basis set. Geometry optimizations were performed in an aqueous environment, which was described through a simple Self Consistent Reaction Field (SCRF) method. More specifically, the Polarizable Continuum Model[35,36] (PCM) was used in the framework of the B3LYP/6-31++G(d,p) level. No symmetry constraints were used in the geometry optimizations.

Cell culture assays

Cell culture maintenance. All cell culture reagents were purchased from Thermo Fisher Scientific. Vero cells (kidney epithelial cells from African green monkey) were cultured in T-flasks (75 cm^2) in Roswell Park Memorial Institute (RPMI) medium supplemented with 10% fetal bovine serum (FBS) and 1% antibiotic/antimycotic solution (penicillin (100 units per mL), streptomycin (100 μg mL^{-1}), and amphotericin (25 μg mL^{-1})), at 37 °C under 5% CO_2 (changing the medium every 2 days). The cells were passaged at 90% confluence by incubation with trypsin-EDTA 0.25% solution for 3 min at 37 °C and sub-cultured at a 1 : 4 split ratio.

Cell viability assays. The tested samples were placed in tissue culture polystyrene (TCP) well plates and sterilized using UV irradiation for 30 min in a laminar flow hood. The contact of cells with the products derived from the samples was promoted through Transwell inserts, which consist of a holder that is placed inside a well with a membrane on the bottom, allowing the transfer of molecules between the hydrogel sample and the cells that are at the bottom of the well. Cytotoxicity of the degradation products was assessed after 1-day (adhesion) and 7-day (proliferation) incubation periods. The cells were seeded at a density of 2×10^4 cells per well and 5×10^4 cells per well, respectively, in 24-well plates and incubated with the samples for 24 h or 7 days in a humidified incubator under an atmosphere of 5% CO_2 and 95% O_2 at 37 °C. Cellular viability was evaluated by the colorimetric MTT [3-(4,5-dimethylthiazol-2-yl)-2,5-diphenyltetrazolium bromide] assay. Specifically, after discarding the medium, 1 mL of MTT solution (5 mg mL^{-1} in medium) was added to each well in the 24-well plates. After 3 h of incubation at 37 °C, the medium was discarded and 1 mL of dimethyl sulfoxide (DMSO) was added to each well to dissolve formazan crystals. Finally, the absorbance was measured using a plate reader at 570 nm. The viability results correspond to the average of three independent replicas (n = 3) for each system. The results were normalized to the control (TCP), for relative percentages. Statistical analyses were performed with a confidence level of 95% (p < 0.05) using Student's T-test.

Confocal microscopy. After the incubation period, the cells were fixed using 2.5% glutaraldehyde solution in PBS, and stained with Alexa Fluor 488 phalloidin and Hoechst dye for visualizing the actin cytoskeleton and the nuclei, respectively. The samples were protected from light and kept at 4 °C before imaging, which was performed using a 10× objective of an Axio Observer 7 Confocal laser microscope (Carl ZEISS LSM 800, Germany). Image processing was completed using ZEN software (ZEISS, Germany), and ImageJ software (Wayne Rasband, NIH, USA).

Migration assay. To assess the potential of cell migration through the core of the selected microtubular construct, only half of the volume of the microtube was filled with hydrogel. For this purpose, the microtubular construct was firstly steri-

lized using UV irradiation for 30 min in a laminar flow hood. Then, half of the microtube was filled with the clickHA hydrogel, which was prepared as described above (*i.e.*, injecting the HA-SH : $PEG_{3\text{-arm}}$ mixture with the pH adjusted to 7.4), and further sterilized using UV irradiation for 30 min in a laminar flow hood. After that, a sterile HA-SH solution (31.3 mg in 150 μL PBS) was prepared and mixed with 150 μL of cell suspension to a final concentration of 2×10^6 cells per mL. The HA-SH solution with cells was then injected into the empty half of the nanotube. The objective of the cell migration assay is sketched in Scheme 1. Thus, what is expected is that the cells introduced into the HA-SH solution migrate to the interface of the clickHA hydrogel because they are in a more comfortable environment.

The LIVE/DEAD viability assay was performed after 1 h, 24 h, 48 h and 6 days of incubation. The cells were stained with 0.5 μL mL^{-1} of calcein stock solution (green for live cells) and 2 μL mL^{-1} of ethidium bromide stock solution (red for dead cells) for 1 h, and washed 3 times with the cell medium. Imaging of the samples was performed using the procedure and equipment described above for cell viability assays.

Results and discussion

Self-standing PLA/PCL films

PLA/PCL blends were prepared using three different PLA : PCL weight ratios (90 : 10, 70 : 30, and 50 : 50). These compositions were chosen considering previous studies on macroscopic samples that showed how the stiffness and tensile strength of the blends gradually decreased with the PLA content, while the elongation at break increased.[26] Thus, these three compositions provide a complete representation of PLA/PCL blends with different mechanical properties. In this work, self-standing 90 : 10, 70 : 30 and 50 : 50 PLA/PCL microfilms were prepared using the corresponding PLA : PCL mixtures in 2 : 1 chloroform : acetone and employing the process schematically depicted in Fig. 1a. This is a four-step process: (1) spin-coating a sacrificial PVA layer onto a stainless steel substrate; (2) spin-coating a PLA/PCL layer onto the sacrificial layer; (3) cutting the deposited membrane (2.5×2.5 cm^2) into three equal membranes of 0.83×2.5 cm^2; and (4) converting the supported membranes into self-standing submicrometric films by dissolving the PVA sacrificial layer.

PLA/PCL blends are thermodynamically immiscible and exhibit poor interfacial adhesion between phases, which is known to affect their mechanical performance.[37,38] In order to investigate this low degree of miscibility in thin films, the surface topography and phase distribution of the prepared spin-coated films (90 : 10, 70 : 30 and 50 : 50 PLA : PCL mixtures) were studied using AFM (Fig. 1b). As it can be seen, surface irregularities, which appear as PCL raised craters dispersed on a relatively flat PLA film, increase with the amount of PCL, which indicates the formation of PCL droplets during the spin-coating process. Furthermore, the size of such droplets, which was attributed to the poor interfacial adhesion between the two polymers, increases from ~1 μm to ~3 μm in diameter with the content of PCL. On the other hand, phase images allowed us to clearly distinguish between two phases in the blend, even though detailed inspection evidences some dissolved PLA in the PCL droplets close to the interface regions. The coexistence of PLA and PCL indicates that the adhesion between the two phases at the interface region was low but non-null in spin-coated films.

The thickness of PLA/PCL films was evaluated by both AFM scratching tests, using the tip in the contact mode, and optical profilometry. The thickness as determined by AFM was around 0.7–0.8 μm in all cases (*i.e.*, the average thickness obtained considering 3 independent films ranged from 739 ± 86 nm for PLA/PCL 50 : 50 to 748 ± 60 nm and 788 ± 65 nm for PLA/PCL 90 : 10 and 70 : 30, respectively). Fig. S1† shows representative AFM height images of scratched PLA/PCL 90 : 10, 70 : 30 and 50 : 50 films and the cross-sectional height profiles associated with such images. On the other hand, optical profilometry confirmed the submicrometric thickness of the prepared films. Thus, the thickness values obtained by this technique (589 ± 129, 603 ± 183, and 968 ± 178 nm for PLA/PCL 90 : 10, 70 : 30 and 50 : 50 films, respectively) were in agreement with those determined by AFM.

The FTIR spectra of submicrometric PLA/PCL films are compared in Fig. 2a with those of films obtained using neat PLA and PCL. The spectrum of PLA shows the characteristic bands, the main ones referring to C–O stretching (1080 cm^{-1}), bending for CH_3 symmetric and asymmetric (1362 and

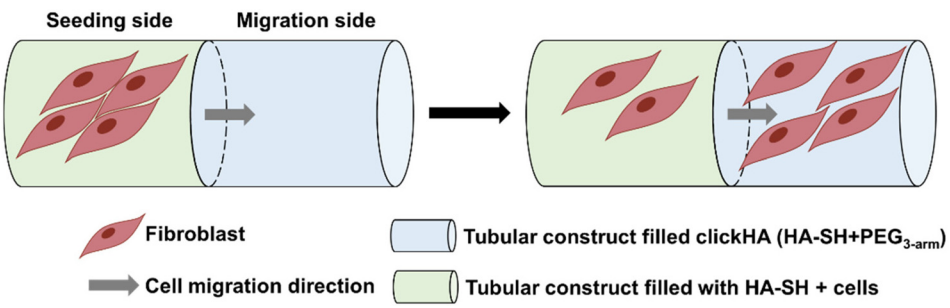

Scheme 1 Sketch describing the cell migration assay.

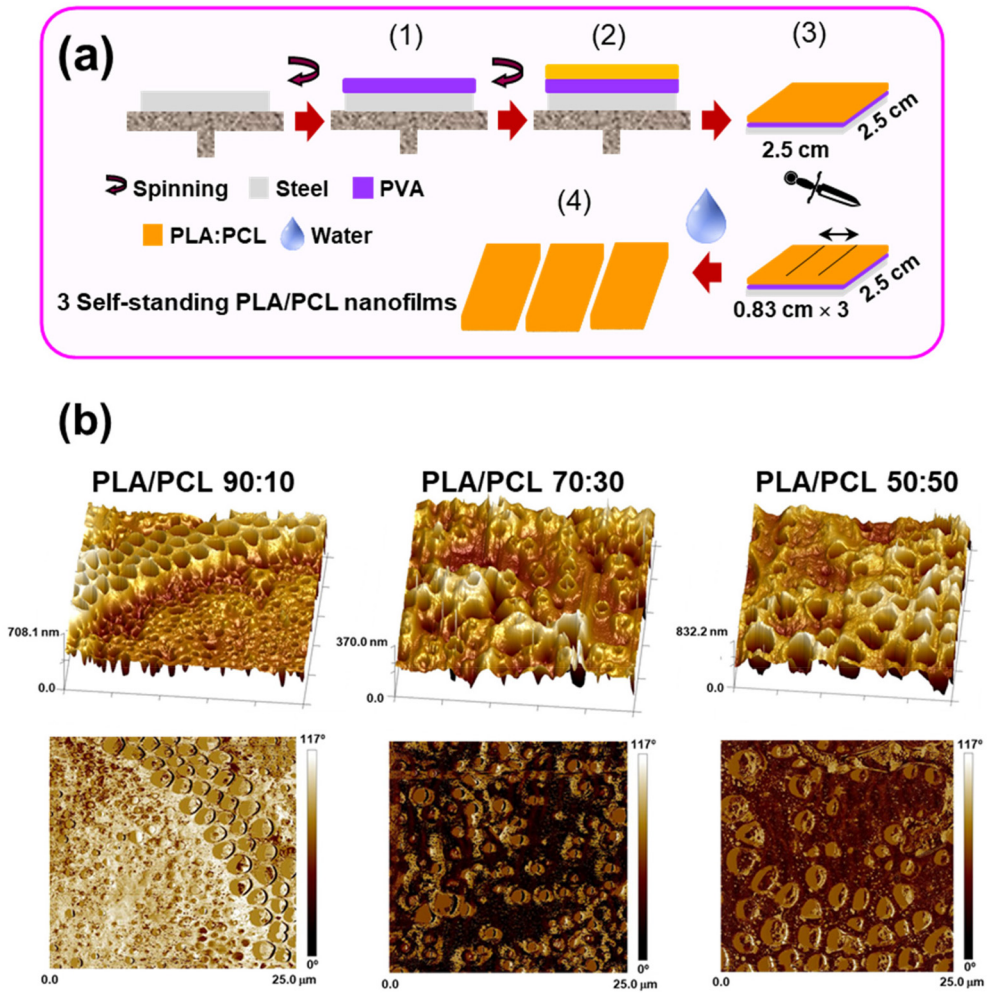

Fig. 1 (a) Scheme showing the process used to prepare self-standing PLA/PCL films of submicrometric thickness. (b) Representative topography (top) and phase (bottom) AFM images (25 × 25 μm^2) of PLA/PCL 90 : 10, 70 : 30 and 50 : 50 films.

1454 cm^{-1}, respectively), C═O stretching (1747 cm^{-1}), and CH_3 symmetric and asymmetric stretching (2942 and 2993 cm^{-1}, respectively). Many of the peaks identified for neat PCL appear at similar wavenumbers, for example, those associated with the C–O stretching (1044 cm^{-1}), C═O stretching (1722 cm^{-1}), and CH_2 symmetric and asymmetric stretching (2864 and 2944 cm^{-1}, respectively). For the PLA/PCL blends, the spectra are similar to those of neat PLA and PCL. For example, the presence of both PLA and PCL in 50 : 50 and 70 : 30 PLA/PCL films is clearly confirmed by the co-existence of the C═O peaks at 1747 and 1722 cm^{-1}. Instead, 90 : 10 PLA/PCL films only show the PLA C═O stretching band, the presence of PCL being evidenced by the CH_2 stretching bands that show reminiscences of those of the latter polyester.

Fig. 2b displays the Raman spectra recorded for films derived from neat polymers and blends. For PLA, fingerprints appear at 873 cm^{-1} (C–COO vibration), 1044 cm^{-1} (C–CH_3 stretching), 1130 cm^{-1} (CH_3 asymmetric groups), 1302 and 1458 cm^{-1} (symmetric and asymmetric CH_3 deformation mode, respectively), 1771 cm^{-1} (strong C═O groups), and 2882–3001 cm^{-1} (C–H stretching modes of CH_3 and CH).[39] PCL shows the characteristic peaks at 922 cm^{-1} (C–COO vibration), 1111 cm^{-1} (skeletal stretching), 1286–1307 cm^{-1} (ωCH_2), 1442 cm^{-1} (CH_2 vibrations), 1724 cm^{-1} (strong C═O groups), and 2864–2915 (C–H stretching modes of CH_2).[40] Inspection of the Raman spectra recorded for 90 : 10, 70 : 30 and 50 : 50 PLA/PCL blends reveals that the intensity of the bands attributed to CH_3 vibrations decreases with increasing PCL content, while the C═O stretching peak splits proportionally to the amount of each polymer in the blend, which corroborates the presence of both PLA and PCL. Overall, the results displayed by FTIR and Raman spectra were fully consistent.

XRD patterns of PLA/PCL films of submicrometric thickness, prepared as previously described (Fig. 1a), are shown in Fig. 3. The three systems show two characteristic peaks at 2θ = 21.4° and 23.8°, which are characteristic of the (110) and (200) reflections from semi-crystalline PCL.[41] The intensities of such peaks were lowered by increasing the amount of PLA. No characteristic peak of crystalline PLA, which usually appears at around 2θ = 15°, 16° and 19°,[42] was detected, suggesting that

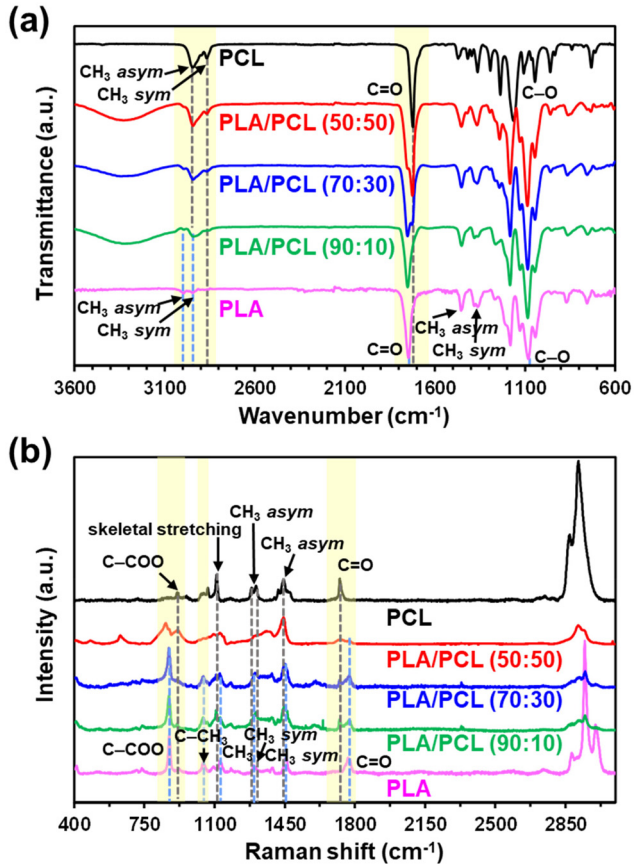

Fig. 2 (a) FTIR and (b) Raman spectra of films derived from neat PLA, 90 : 10 PLA/PCL, 70 : 30 PLA/PCL, 50 : 50 PLA/PCL and neat PCL.

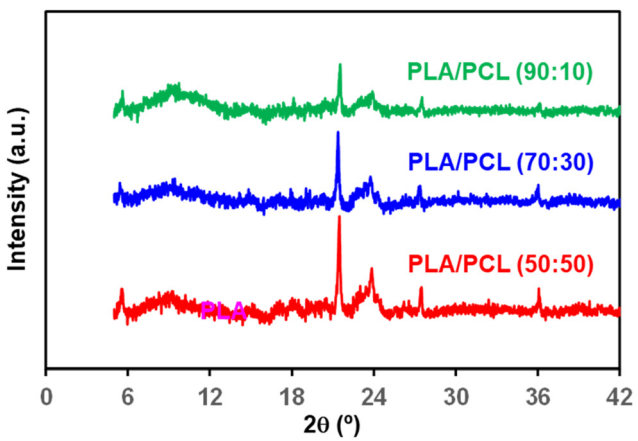

Fig. 3 XRD patterns of 50 : 50, 70 : 30 and 90 : 10 PLA/PCL films of sub-micrometric thickness.

the PLA phase remains mainly amorphous in the three blends. This hypothesis is consistent with the variation of the crystallinity, χ_c, which decreases with increasing PLA content. Thus, the values of χ_c were 0.22, 0.25 and 0.29 for 90 : 10, 70 : 30 and 50 : 50 PLA/PCL.

Representative stress–strain curves of neat PLA, PLA/PCL blends and neat PCL are shown in Fig. S2,† while the elastic modulus (E), tensile strength (σ_{max}) and elongation at break (ε_{break}) values, averaged over eight samples, are listed in Table 1. The elastic modulus was higher for neat PLA than for the blends and neat PCL, the values for PLA/PCL blends decreasing with increasing amount of PCL. Moreover, the elastic modulus of PLA/PCL 50 : 50 was around 30% lower than that of neat PCL, which was attributed to the well-known immiscibility between PLA and PCL.[43] This effect was minimized in PLA/PCL 90 : 10 and 70 : 30, whose elastic moduli were 49% and 73% lower than that of neat PLA, respectively, but 142% and 30% higher than that of neat PCL, respectively. This behavior indicated that, while PLA/PCL 50 : 50 was dominated by the immiscibility between the two polymers, the partial interfacial adhesion between the two phases prevailed in PLA/PCL 90 : 10 and 70 : 30, allowing the transfer of stress and failure energy and, therefore, improving the mechanical resistance with respect to neat PCL. This behavior was consistent with the elongation at break, which increased with the amount of PCL, and with the tensile strength that was higher for some of the blends than for neat PLA and PCL. Thus, partial interfacial adhesion blocked the propagation of the mechanical fracture between the PLA and PCL phases in the blends.

Tubular constructs

Tubular constructs were fabricated using the shape memory effects, as described in the Methods section. For this purpose, self-standing PLA/PCL microfilms were heated at 60 °C for 1 min and, subsequently, rolled along a PLA rod (Fig. S3a†). Then, the microfilms, which formed a spiral around the rod (Fig. S3b†), were immersed in a water bath at room temperature to fix the shape. Finally, the tubes were detached from the rod with the help of tweezers (Fig. S3c†), becoming self-standing. Fig. S3d† shows a representative tubular construct after the whole process, which is illustrated in the ESI (Video S1†).

ClickHA hydrogel and filling of tubular constructs

The clickHA hydrogel was selected to fill microtubular constructs since its Young's modulus (10.8 ± 0.9 kPa)[29] is very similar to that reported for human peripheral nerves (9.5–10.4 kPa).[44] Furthermore, such a hydrogel, which is obtained by mixing HA-SH and $PEG_{3\text{-arm}}$ solutions in PBS and adjusting

Table 1 Mechanical properties of the neat PLA, neat PCL, and PLA/PCL blends: elastic modulus (E), tensile strength (σ_{max}) and elongation at break (ε_{break})

	PLA	PLA/PCL (90 : 10)	PLA/PCL (70 : 30)	PLA/PCL (50 : 50)	PCL
E (MPa)	2051 ± 122	1041 ± 220	557 ± 92	286 ± 73	430 ± 64
σ_{max} (aMPa)	48 ± 2	44 ± 3	85 ± 5	84 ± 11	45 ± 14
ε_{break} (%)	3.9 ± 0.3	97 ± 15	122 ± 31	293 ± 39	691 ± 43

the pH to 7.4 with KOH,[28,29] is mechanically stable, as determined by rheological characterization.[28]

In this work, after examining different options with preliminary assays, the hydrogel was confined inside the tubes by gelling *in situ*. For this purpose, the mixture of HA-SH : $PEG_{3\text{-arm}}$ precursors at the selected pH, which was adjusted by adding KOH, was carefully introduced into the tubular constructs immediately after pH adjustment. The gelation time was optimized, minimizing it by adjusting the [KOH]/[HA-SH] concentration ratio. As is shown in Fig. 4a, the gelation time increases with decreasing [KOH]/[HA-SH] ratio. Indeed, the gelation was practically immediate (≤60 s) when the ratio was between 0.1 and 0.075. Accordingly, a [KOH]/[HA-SH] ratio of 0.075 was considered to achieve fast gelation inside the microtubular constructs.

To confirm the successful formation of the clickHA hydrogel inside the microtubular constructs, the latter was carefully removed, and the FTIR spectrum of the collected clickHA hydrogel was acquired (Fig. 4b). As it can be seen, the absorption peaks corresponding to the stretching of the C–O–C group (1020 cm^{-1}), asymmetric C═O and symmetric C–O stretching modes of the COO^- groups (1647 and 1558 cm^{-1}, respectively), stretching vibration of C–H (2917 cm^{-1}), and stretching vibration of O–H and N–H groups (3400 cm^{-1}), were observed.[45]

The surface hydrophobicity/hydrophilicity of the PLA/PCL tubular microconstructs filled with the clickHA hydrogel was determined by measuring the water contact angle (WCA) using the sessile water droplet method. The resulting WCA values were 68° ± 7°, 90° ± 8° and 78° ± 7° for 50 : 50, 70 : 30 and 90 : 10 filled microtubes, respectively. The values reported for hot-pressed 50 : 50, 70 : 30 and 90 : 10 PLA/PCL films were 57° ± 11°, 59° ± 9° and 64° ± 5°, respectively.[26] This comparison indicates that the wettability of the tubular microconstructs is largely influenced by the surface topography, which in turn not only depends on the preparation process but also is significantly affected by the hydrogel confined inside (see below).

On the other hand, Fig. 5 shows cross-section SEM micrographs of the 50 : 50, 70 : 30 and 90 : 10 PLA/PCL tubular constructs filled with hydrogels. Two representative micrographs are displayed for each case. The first one (left panel) confirms that the hydrogel is well integrated inside the microtubes, independently of their composition, while the second one (right panel) confirms that the general honeycomb morphology of the hydrogel is not altered by the confinement. This morphology reflects the formation of pseudo-circular pores with a smooth surface, with an average diameter that depends on the composition of the blend construct. Thus, the average diameter increases from 11.1 ± 2.7 μm for the 50 : 50 PLA/PCL system to 34.4 ± 12.9 and 57.6 ± 13.2 μm for the 70 : 30 and 90 : 10 PLA/PCL ones, respectively. This observation indicates that the mechanical properties of the PLA/PCL shell affect the sizes that ice crystals can grow to during the freezing process of the confined hydrogel. The whole process, including the mixture of HA-SH : $PEG_{3\text{-arm}}$ precursors, its injection in the tubular construct and the gelation of the clickHA hydrogel inside a microtubular construct, are shown in the ESI (Video S2†).

The porosity of the lyophilized clickHA hydrogel in 50 : 50, 70 : 30 and 90 : 10 microtubular constructs was studied using μ-CT (Table 2 and Fig. 6). Both pore size distributions and cross-section images confirmed SEM observations (Fig. 5), which indicated a dependence on the tubular construct composition. The total porosity and the interconnection among the pores are higher for the hydrogel confined in the 70 : 30 PLA/PCL microtube than in the other two constructs. Table 2 quantifies the percentage of each type of porosity (*i.e.*, the pore interconnectivity), which has been categorized as open, closed and total, the latter being the sum of the open and closed ones. Open pores are associated with the interconnected structure formed by the network of connected pores, while closed pores refer to those that do not contribute to the accessible pore structure (*i.e.*, unconnected ones). The total porosity and the percentage of open pores were around 6% and 11% higher for the hydrogel confined in the 70 : 30 construct than for the hydrogels confined in the 50 : 50 and 90 : 30 tubes, respectively. The closed porosity was higher for the hydrogel filling the 90 : 30 PLA/PCL construct. It is worth noting that the open porosity is the most significant type of porosity since it enables fluids to flow through the material. Remarkably, the porosity

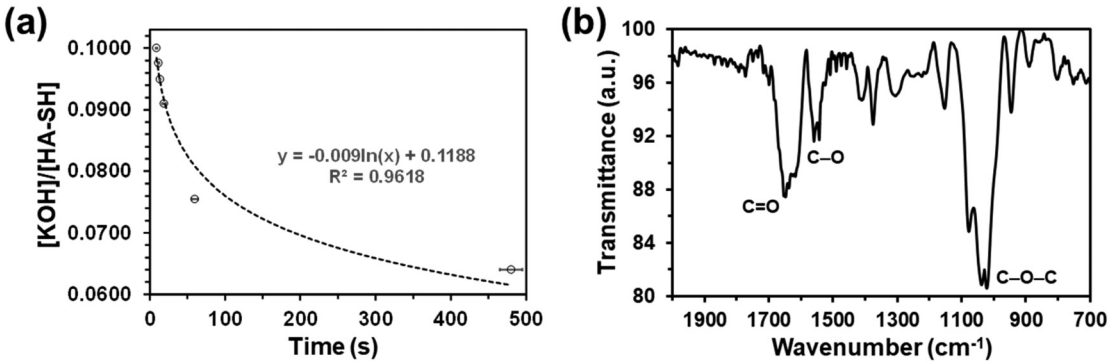

Fig. 4 (a) Variation in the gelation time against the [KOH]/[HA-SH] ratio. (b) FTIR spectrum of the clickHA hydrogel obtained after removing the 70 : 30 PLA/PCL tubular construct.

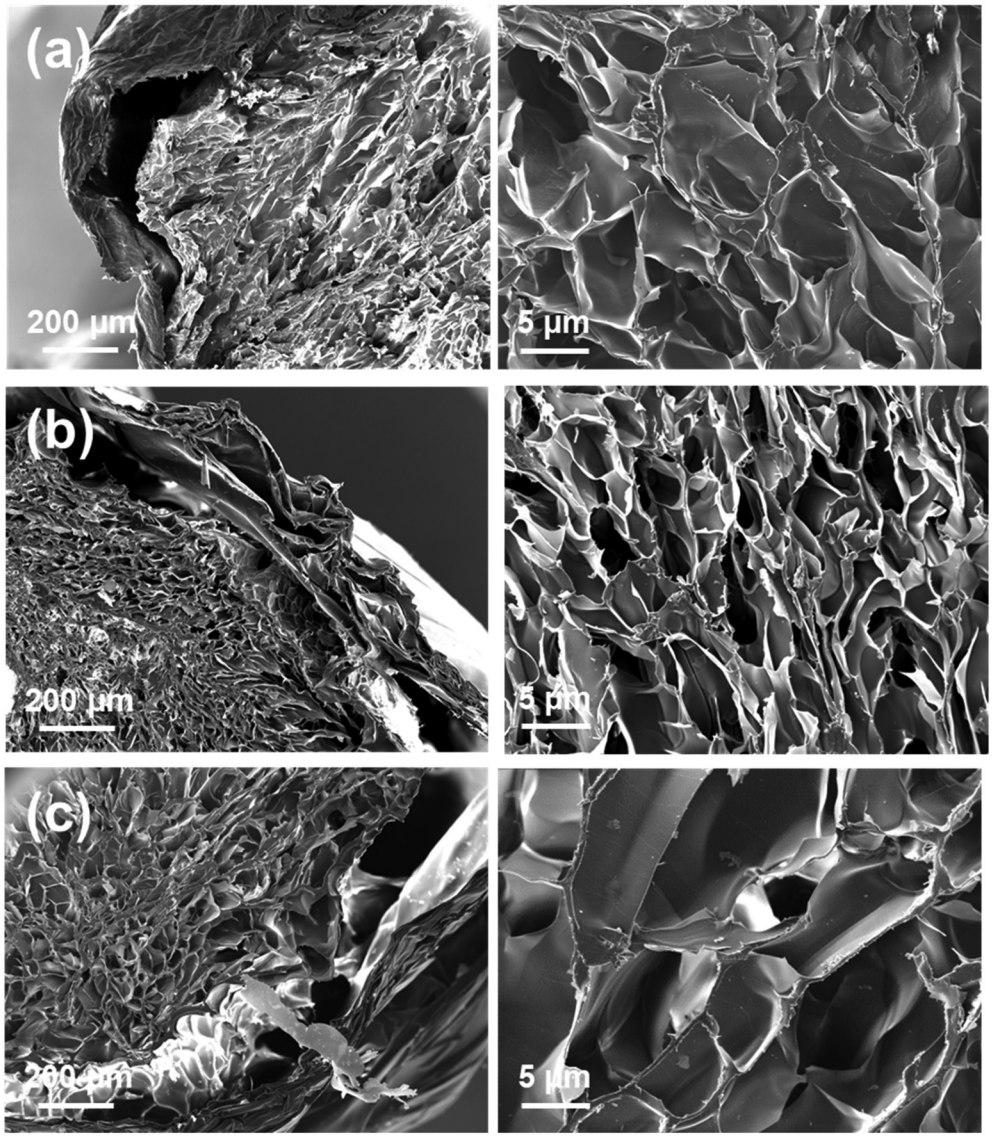

Fig. 5 Cross-section SEM images of (a) 50 : 50, (b) 70 : 30 and (c) 90 : 10 microtubular constructs filled with the clickHA hydrogel. Images showing the integration of the clickHA hydrogel and the PLA/PCL shell (left) and the honeycomb morphology of the clickHA hydrogel (right) are shown.

Table 2 Porosity (in %) of lyophilized clickHA hydrogel 50 : 50, 70 : 30 and 90 : 10 microtubular construct filled samples

Construct	Total	Closed	Open
50 : 50 PLA/PCL	60.7	0.1	60.6
70 : 30 PLA/PCL	66.8	<0.06	66.8
90 : 10 PLA/PCL	56.2	0.2	56.3

of the clickHA hydrogel was largely dominated by open pores, independently of the composition of the construct used to confine it.

μ-CT images of the confined hydrogels are displayed in Fig. 6. In general, the pores of the filling hydrogel were aligned with the axis of the construct in all cases, which was expected to favor cell migration across the tube. On the other hand, the average pore size determined by μ-CT was 28.4 ± 14.3, 46.6 ± 17.0 and 55.2 ± 16.9 μm for the hydrogels contained in the 50 : 50, 70 : 30 and 90 : 10 PLA/PCL systems, respectively. These values were consistent with those estimated from cross-section SEM images.

In order to ascertain the dominant interactions in PLA/PCL tubular constructs filled with clickHA, DFT calculations were performed considering PLA, PCL and HA model chains constituted by 5, 3 and 2 repeat units, respectively. Such amounts of repeat units were chosen to facilitate the comparison among the binding energies (ΔE_b) of the complexes used to model such three-component systems (*i.e.*, the model chains of the three compounds displayed a similar number of atoms). Before constructing the PLA···PCL, PLA···HA and PCL···HA assemblies, the geometry of the three individual model chains was optimized. At least 20 model complexes involving pairs of

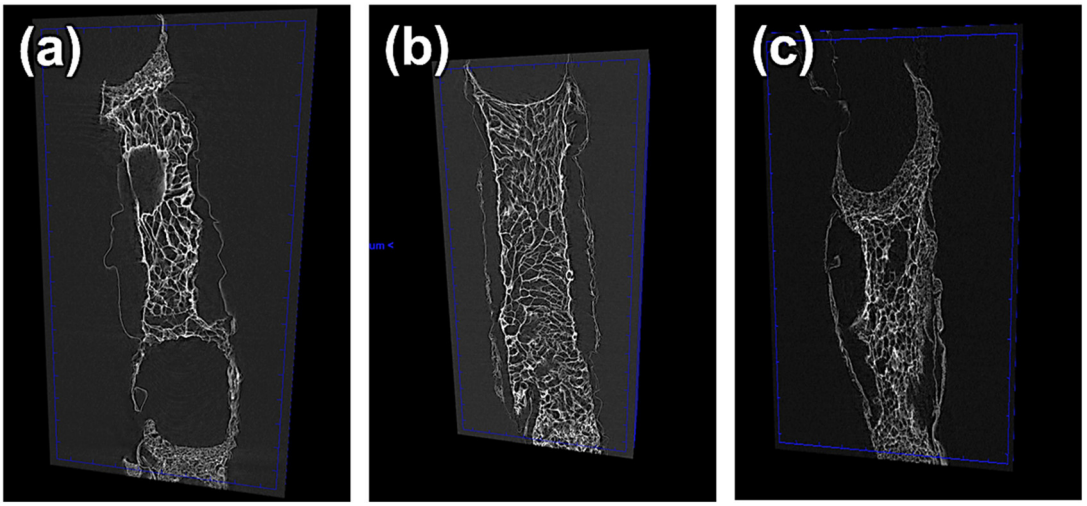

Fig. 6 μ-CT images of the clickHA hydrogels confined in (a) 50 : 50, (b) 70 : 30 and (c) 90 : 10 PLA/PCL tubular constructs.

two model chains were constructed. They differed in the relative arrangement between the two interacting components, which was substantially changed. All model complexes were optimized in a surrounding aqueous environment at the PCM-B3LYP/6-311++G(d,p) level.

Fig. 7 displays the lowest energy complex computed for PLA···PCL, PLA···HA and PCL···HA assemblies, with the corresponding ΔE_b values also displayed. As it can be seen, the interaction between PLA and PCL was extremely weak (ΔE_b = −1.0 kcal mol^{-1}), which was associated with the lack of groups

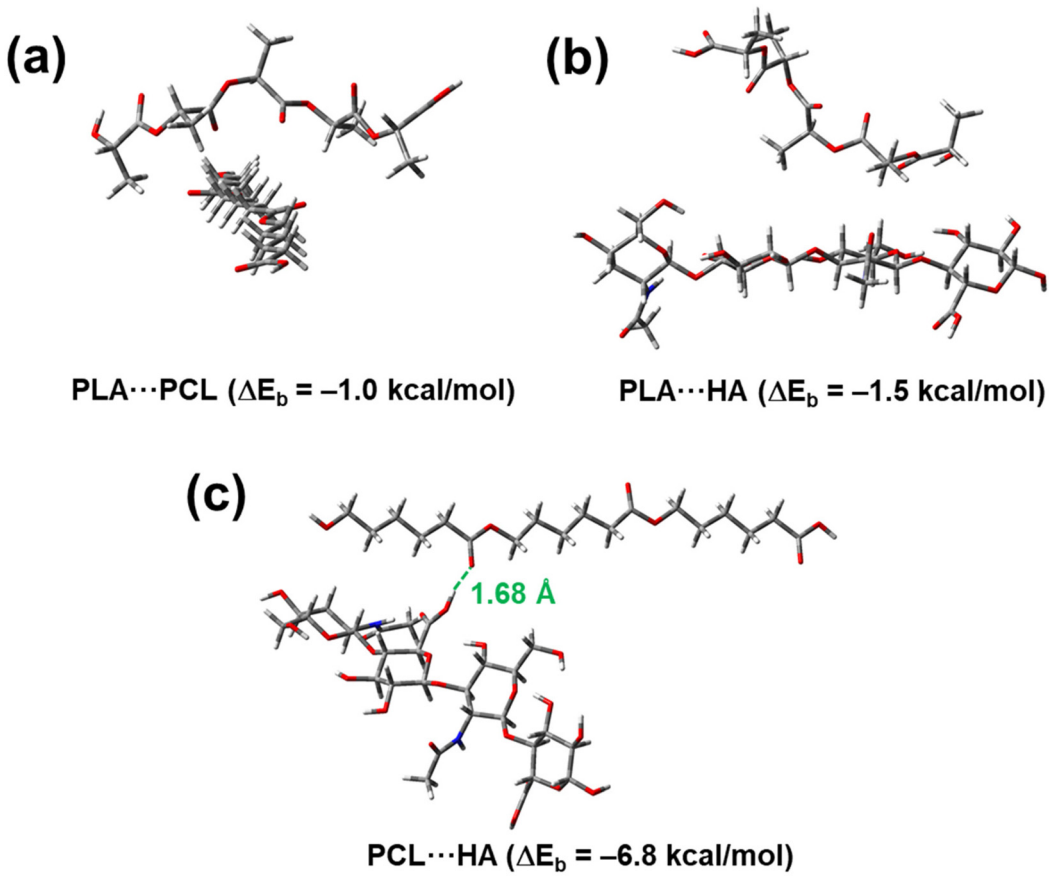

Fig. 7 Lowest energy assemblies found for (a) PLA···PCL, (b) PLA···HA and (c) PCL···HA complexes. Binding energies (ΔE_b) are also shown.

able to act as hydrogen bonding donors (Fig. 7a). Indeed, the two model chains interact through weak non-specific van der Waals interactions, which is consistent with the experimentally observed poor interfacial adhesion between PLA and PCL phases.[37,38] On the other hand, HA contains hydrogen bond donors, suggesting that the binding should be much stronger in PLA···HA and PCL···HA assemblies.

Interestingly, PLA···HA and PCL···HA complexes exhibited very different behavior. While the formation of hydrogen bonds was restricted in PLA···HA by the methyl side group of each PLA repeat unit (Fig. 7b), such steric effect did not exist in PCL···HA, giving place to the formation of strong (O–)H···O=C hydrogen bonds with a H···O distance of 1.7 Å only (Fig. 7c). As a consequence, the ΔE_b value obtained for PLA···HA was only slightly higher than that for PLA···PCL (−1.5 kcal mol^{-1} *vs.* −1.0 kcal mol^{-1}). The small difference between the two complexes was attributed to the dipole–dipole interaction, since the dipole moment was higher for PLA and HA (6.8 and 7.8 Debyes, respectively) than for PCL (5.0 Debyes). Instead, the strength of the binding between PCL and HA model compounds increased to ΔE_b = −6.8 kcal mol^{-1}, which is close to the values typically found for strong hydrogen bonds.[46,47] Overall, these results indicated that the adhesion of the clickHA hydrogel to the inner walls of the PLA/PCL shell is probably influenced mainly by the interactions with the PCL domains.

The mechanical performance of 50 : 50, 70 : 30 and 90 : 10 PLA/PCL tubular constructs filled with the clickHA hydrogel was assessed by uniaxial compression testing (Fig. 8a). The overall response of the three filled constructs was similar to that of the clickHA hydrogel alone (control), indicating that the PLA/PCL microtubes do not induce any stiffening effect. This is corroborated in Fig. 8b, which compares the elastic modulus of the filled constructs and the control. Thus, the elastic modulus of the clickHA hydrogel, which was 18.3 ± 1.5 kPa, remained around 19 kPa when it was confined inside the microtubular constructs (*i.e.*, 18.7 ± 3.6, 19.2 ± 2.9 and 19.6 ± 5.3 kPa for the filled 50 : 50, 70 : 30 and 90 : 10 PLA/PCL con-

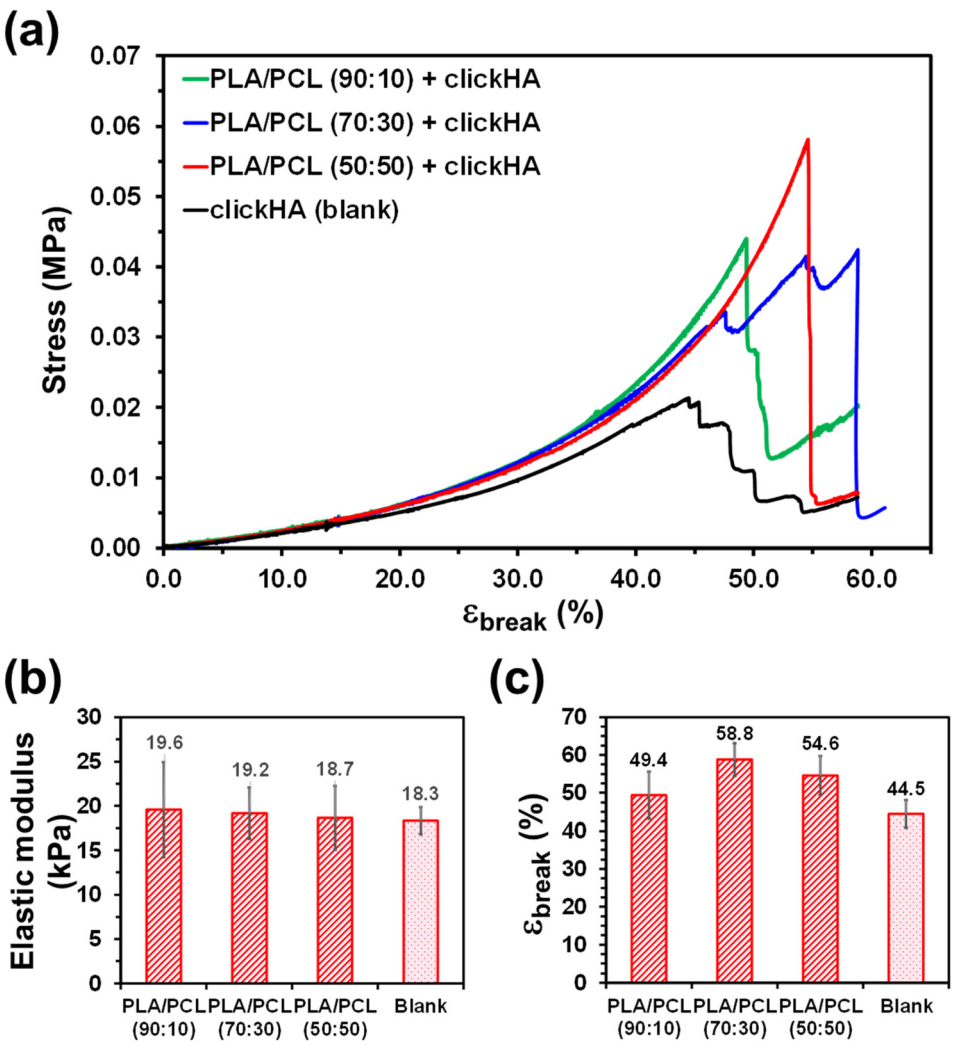

Fig. 8 (a) Representative uniaxial compressive curves for the clickHA hydrogel alone and clickHA-filled 90 : 10, 70 : 30 and 50 : 50 PLA/PCL microtubular constructs. Comparison of the (b) elastic modulus (E) and (c) elongation at break (ε_{break}) values.

structs, respectively). Furthermore, this value was similar to that previously determined for the non-confined hydrogel at 37 °C.[48]

Fig. 8a also indicates that the ultimate compressive strength, which corresponds to the maximum stress that a material can withstand while being compressed before breaking, was significantly higher for the hydrogel confined inside the tubular microconstructs than for the free hydrogel, indicating that the strength of PLA/PCL tubes enhanced that of the hydrogel. Accordingly, the elongation at break of the blank click hydrogel was lower than those of the PLA/PCL tubes with the confined hydrogel, as is shown in Fig. 8c.

DSC thermograms recorded for the second heating of PLA/PCL tubular constructs filled with the clickHA hydrogel are compared in Fig. 9a. The PLA glass transition temperature is observed at T_g = 57–60°, while the melting temperature appears at T_m = 155 °C. Besides, a peak that has been attributed to the melting crystallization of PCL, appears at around 25 °C. These transition temperatures are very similar to those recorded for neat PLA and PCL,[26] confirming that PLA and PCL are immiscible.

The TGA thermograms of 50 : 50, 70 : 30 and 90 : 10 PLA/PCL microtubes filled with clickHA are displayed in Fig. 9b. The decomposition of PLA and PCL occurs at around 370 and 410 °C, respectively.[26] Due to the poor miscibility of the two polyesters, these decomposition temperatures are maintained in microstructures without clickHA.[26] However, the thermograms displayed in Fig. 9b show that the decomposition temperature of PCL shifts to a lower value, especially in the case of 90 : 10 PLA/PCL tubes (*i.e.*, 395 °C), while that of PLA is preserved at 370 °C. This shifting is consistent with the fact that clickHA, which decomposes at around 250 °C, tends to interact with PCL, as was reflected in theoretical calculations (Fig. 7).

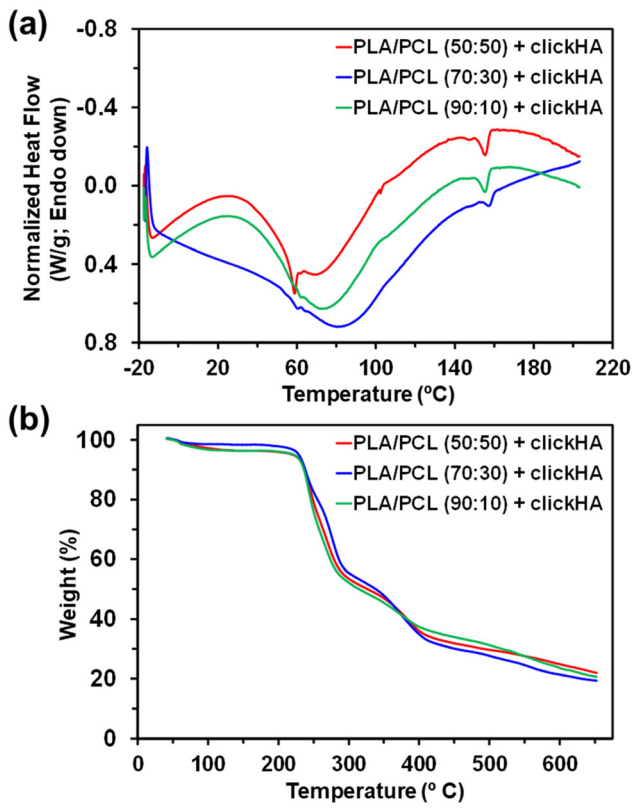

Fig. 9 (a) DSC analyses (second heating scan) and (b) TGA thermograms of PLA/PCL microtubular constructs filled with the hydrogel.

On the other hand, in the previous study,[28] we found that, although the degradation of non-confined clickHA was relatively fast (~21 days for show a weight loss > 80%), even after 7 days the hydrogel was stable enough to be handled. However, the degradation of clickHA confined in PLA/PCL constructs is significantly slower due to the protection imparted by the walls of the tube, since after 7 days hardly any signs of degradation were observed in either the tubes or the hydrogel.

Cytocompatibility

The cytocompatibility of released products from the PLA/PCL blends, the clickHA hydrogel matrix, and the tubular constructs filled with clickHA was investigated by assessing the viability of Vero cells at 24 h and 7 days of cell culture. Vero cells are recommended for cytotoxicity, adhesion and proliferation evaluations, as well as to assess the interactions between the cell and the substrate.[49,50] Moreover, Vero cells have been widely used to study the biocompatibility of substrates fabricated for nerve guide,[51–53] which is the main focus of this study.

The results are presented in Fig. 10a, including those obtained for the TCP control. After 24 h, the number of adhered cells in contact with the 50 : 50 PLA/PCL blend and the clickHA hydrogel was very similar to that of the TCP control, whereas the 70 : 30 and 90 : 10 PLA/PCL blends and the three clickHA-filled tubular constructs presented up to 35–56% more adherence than the TCP control. This adhesion study showed that none of the materials studied, individually or in combination, contained toxic substances that adversely affect cell attachment to the TCP. In fact, in some cases, cell adhesion was significantly more favorable than in the control, as is reflected by the confocal microscopy images (Fig. 10b).

After the 7-day incubation period, cell viability of clickHA-filled microtubular constructs was intermediate between that of neat clickHA, which exhibited the lowest viability, and those of PLA/PCL blends, which displayed viability similar to that of the control (Fig. 10a). This behavior indicates that the studied synthetic materials do not have any detrimental impact on cell metabolism, thus allowing proper cell growth and proliferation. It is worth mentioning that, although the cell viability reduced with respect to day 1, cell viabilities were higher than 90% in all cases (*i.e.*, it was between 93% for the clickHA hydrogel and 112% for PLA/PCL 90 : 10 films) with statistical significance, which ensures that the three clickHA-filled microtubular constructs are cytocompatible. Cell proliferation is illustrated for all the studied materials by confocal microscopy images (Fig. 10c).

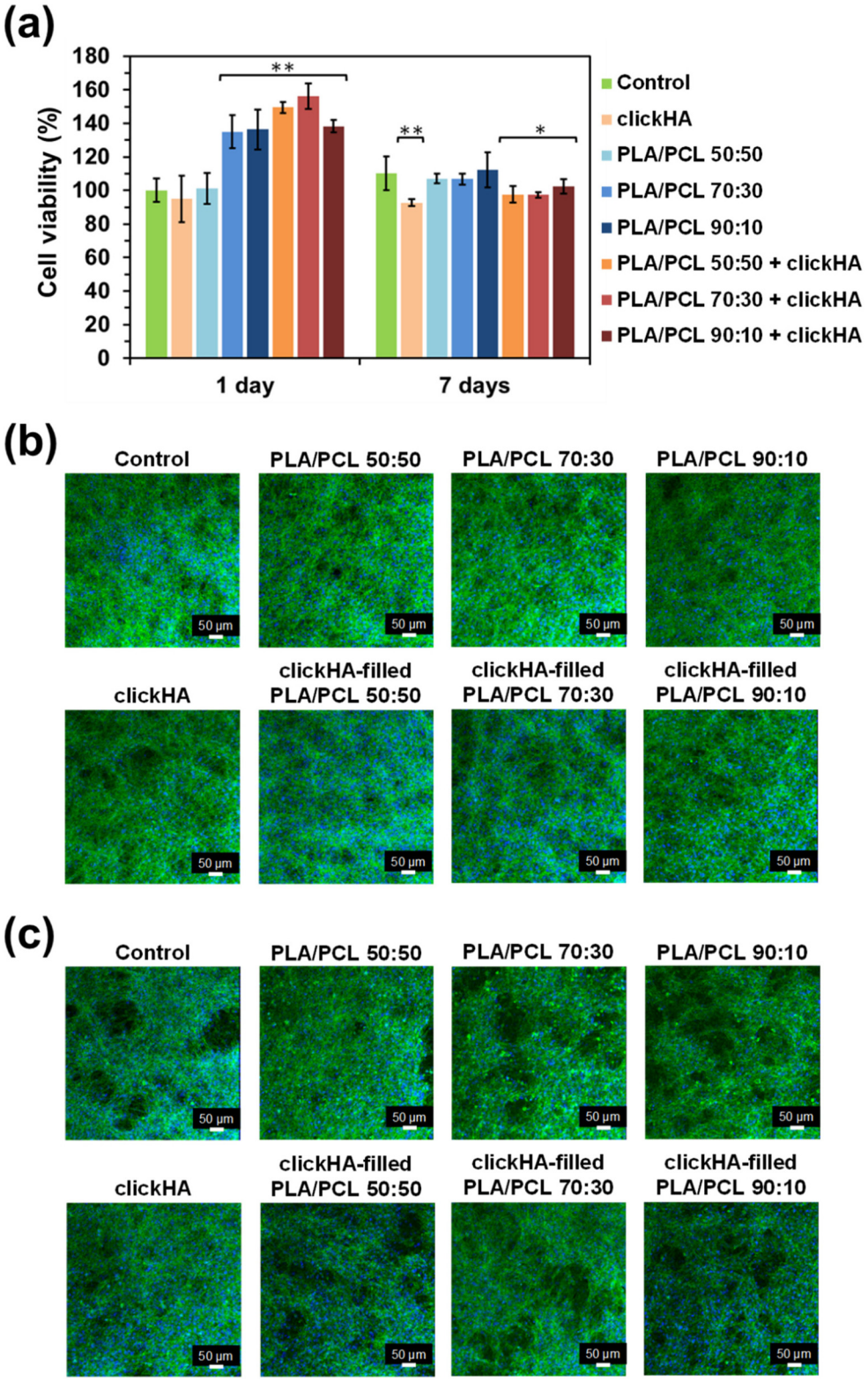

Fig. 10 (a) Cell viability assays for PLA/PCL blends, clickHA hydrogel and hydrogel-filled tubular constructs. (b, c) Confocal microscopy images of the different studied materials and constructs after (b) 1- and (c) 7-day cell incubation periods. Data are represented as mean ± standard deviation; n = 3 per group. Significance levels are as follows: *$p < 0.05$, **$p < 0.01$, determined by one-way ANOVA and Tukey's multiple comparisons test.

Cell migration

The configuration of the tubular constructs used to study cell migration from the HA-SH solution (*i.e.*, seeding area, where cells remain prior to migration) to the clickHA hydrogel (*i.e.*, migration area, where the cells move) is shown in Scheme 1. As the mechanical properties and cytocompatibility of the three considered filled tubes were similar, cell migration assays were only performed considering the 70 : 30 tubular construct, which was considered as representative. Furthermore, considering that the diameter of Vero cells ranges from 12.12 to 14.44 μm (with average cell roundness between 0.73 to 0.75),[54] the average diameter of the clickHA hydrogel confined inside 50 : 50 PLA/PCL tubular constructs was considered too low for this assay. Instead, the difference between the pore diameter of the clickHA hydrogels confined inside the 70 : 30 and 90 : 10 PLA/PCL tubes (34.4 ± 12.9 and 57.6 ± 13.2 μm, respectively, according to μ-CT) was not considered large enough to expect significant differences and, therefore, we chose the most restrictive one.

The clickHA hydrogel, which was cell-free at the beginning of the assay, was confined to half of the 70 : 30 PLA/PCL tubular construct, whereas the second half was filled with a cell-containing HA-SH solution. Although after 1 h, the cells were still predominantly localized in the seeding area, Fig. 11a shows that after 24 h the cells migrated mostly from the HA-SH solution to inside the clickHA hydrogel, which indicates that the tubular construct favors cell movement towards the 3D porous semi-solid environment. Furthermore, the presence of most cells inside the hydrogel was maintained both at 48 h and at 6 days (Fig. 11a), confirming that the movement of cells in the tubular structure is not random but that the cells,

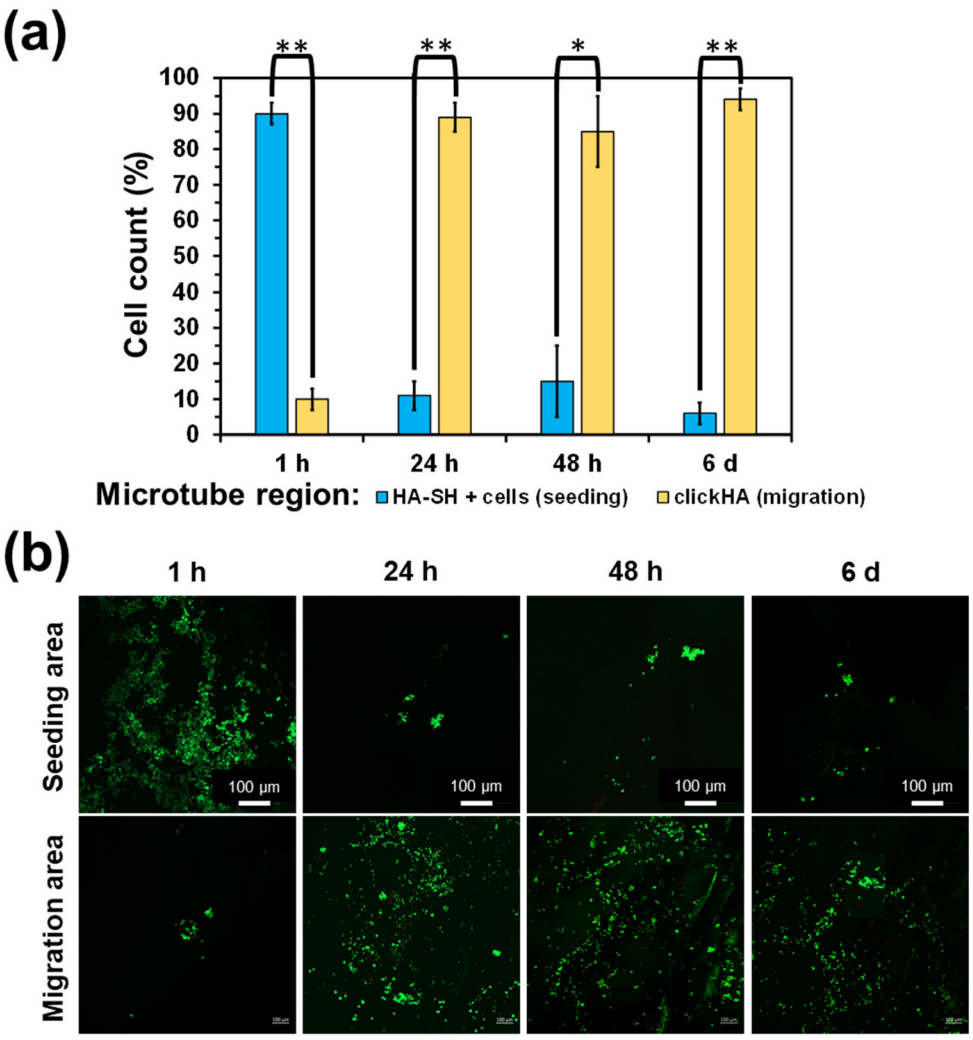

Fig. 11 (a) Cell viability in the migration assay described in Scheme 1. Data are represented as mean ± standard deviation; n = 3 per group. Significance levels are as follows: *p < 0.05, **p < 0.01, determined by one-way ANOVA and Tukey's multiple comparisons test. (b) Confocal microscopy images of the seeding and migration areas after 1 h, 24 h, 48 h and 6 days. The label "seeding area" corresponds to the center of the tubular side filled with HA-SH + cells (seeding side in Scheme 1), while the label "migration area" corresponds to the center of the tubular side filled with clickHA (migration side in Scheme 1).

after moving towards the area where they feel most comfortable, remain there. This result was further supported by confocal microscopy photographs of the seeding and migration areas obtained at different times (Fig. 11b). The average migration distance, which was estimated by analyzing the images using the ImageJ software was 1168 ± 356 μm every 24 h.

Overall, our system (*i.e.*, clickHA hydrogels confined inside 70 : 30 PLA/PCL tubular constructs) supports cell viability and promotes directional cell migration, which evidences its potential for tissue engineering. Indeed, the engineered tubular construct acts as a cylindrical guide that favors cell migration towards the confined hydrogel, thus meeting consistent cell-friendly mechanical conditions. Other PLA/PCL-based scaffolds for nerve regeneration have been recently reported in the literature.[55,56] Mao *et al.*[55] fabricated novel bilayered scaffolds by using electrospun PLA/PCL fibers as the outer layer and extracellular matrix (ECM) as the inner layer. While PLA/PCL fiber offered enough mechanical strength, the ECM promoted the regeneration. The main drawback of such an interesting scaffold was that some important bioactive molecule contents were very low or even lost during the manufacturing process.[55] This is not expected to occur in our system since the loading capacity of hydrogels is very high. On the other hand, clickHA-filled tubular constructs display significant advantages in terms of loading with respect to the approach proposed by Mobasseri *et al.*,[56] which fabricated PLA/PCL films with different shaped grooves that were made using patterned silicon templates. Although those patterned systems showed higher potential than smooth surfaces for regeneration, they only acted as passive conduits without any possibility of loading nutrients or other factors beneficial for regeneration.

Conclusions

Self-standing films of submicrometric thickness were used to fabricate hollow tubular constructs using shape memory PLA/PCL blends. Such structures were filled with a clickHA hydrogel, which was confined inside the tube by gelling *in situ* the injected precursors (HA-SH and $PEG_{3\text{-arm}}$) at pH = 7.4. Although the Young's modulus of the hydrogel was not altered by the confinement in the tubular constructs, the PLA/PCL shell affected the ultimate compressive strength and the strain at break of the confined hydrogel, increasing them. Indeed, the properties of the filled tubular constructs were predominantly influenced by the PCL···HA interactions that were much stronger than those of PLA···PCL and PLA···HA. The engineered constructs were demonstrated to be biocompatible and to promote cell migration in the tubular construct towards the confined hydrogel (*i.e.*, directional migration).

While most existing directional scaffolds are 2D, the ones developed in this study are 3D, reducing the differences with respect to a 3D cellular environment (*i.e.*, cells behave differently in 3D and 2D constructs). Although the engineered device offers valuable insights with implications for directional tissue regeneration, much work is still necessary. Immediate future work will focus, on the one hand, on the incorporation of laminin and/or growth factors into the confined hydrogel to enhance tissue regeneration and, on the other hand, on the fabrication of the proposed scaffolds using a 4D manufacturing technique combining 3D printing with programmed shape transformation.

Conflicts of interest

The authors declare that they have no known competing financial interests.

Data availability

The data supporting this article have been included as part of the ESI.†

Acknowledgements

This publication is part of the I + D + i project PID2021-125767OB-I00 and CEX2023-001300-M funded by MCIN/AEI/10.13039/501100011033 and, as appropriate, by "ERDF A way of making Europe" and European Union Next Generation EU. The authors are thankful to the Agència de Gestió d'Ajuts Universitaris i de Recerca (2021 SGR 00387) for financial support. A. H.-Y. is thankful to the MCIN/AEI for a FPI Fellowship. M. M. P.-M. thanks the Ministerio de Ciencia, Innovación y Universidades for the Junior Beatriz Galindo Award (BG20/00216). Support for the research of C. A. was also received through the prize "ICREA Academia" for excellence in research funded by the Generalitat de Catalunya.

References

1 J. Delaey, P. Dubruel and S. VanVlierberghe, *Adv. Funct. Mater.*, 2020, **30**, 1909047.
2 A. Kirillova and L. Ionov, *J. Mater. Chem. B*, 2019, **7**, 1597–1624.
3 S. Pisani, I. Genta, T. Modena, R. Dorati, M. Benazzo and B. Conti, *Int. J. Mol. Sci.*, 2022, **23**, 1290.
4 W. Zhao, L. Liu, F. Zhang, J. Leng and Y. Liu, *Mater. Sci. Eng., C*, 2019, **97**, 864–883.
5 T. Tadge, S. Garje, V. Saxena and A. M. Raichur, *ACS Omega*, 2023, **8**, 32294–32310.
6 M. R. Pfau and M. A. Grunlan, *J. Mater. Chem. B*, 2021, **9**, 4287–4297.
7 S. M. Hasan, L. D. Nash and D. J. Maitland, *J. Polym. Sci., Part B: Polym. Phys.*, 2016, **54**, 1300–1318.
8 K. Zhang, S. Wang, C. Zhou, L. Cheng, X. Gao, X. Xie, J. Sun, H. Wang, M. D. Weir, M. A. Reynolds, N. Zhang, Y. Bai and H. H. K. Xu, *Bone Res.*, 2018, **6**, 31.

9 N. Sabahi, I. Roohani, C. H. Wang and X. Li, *Addit. Manuf.*, 2025, **98**, 104636.
10 D. Yates, *Nat. Rev. Neurosci.*, 2024, **25**, 142.
11 S. Vijayavenkataraman, *Acta Biomater.*, 2020, **106**, 54–69.
12 R. López-Cebral, J. Silva-Correia, R. L. Reis, T. H. Silva and J. M. Oliveira, *ACS Biomater. Sci. Eng.*, 2017, **3**, 3098–3122.
13 A. B. Lovati, D. D'Arrigo, S. Odella, P. Tos, S. Geuna and S. Raimondo, Nerve Repair Using Decellularized Nerve Grafts in Rat Models. A Review of the Literature, *Front. Cell. Neurosci.*, 2018, **12**, 427.
14 M. Mahar and V. Cavalli, *Nat. Rev. Neurosci.*, 2018, **19**, 323–337.
15 X. Gu, F. Ding and D. F. Williams, *Biomaterials*, 2014, **35**, 6143–6156.
16 M. Anderson, N. B. Shelke, O. S. Manoukian, X. Yu, L. D. McCullough and S. G. Kumbar, *Crit. Rev. Biomed. Eng.*, 2015, **43**, 131–159.
17 M. D. Sarker, S. Naghieh, A. D. McInnes, D. J. Schreyer and X. Chen, *Prog. Neurobiol.*, 2018, **171**, 125–150.
18 M. Mehrpouya, H. Vahabi, S. Janbaz, A. Darafsheh, T. R. Mazur and S. Ramakrishna, *Polymer*, 2021, **230**, 124080.
19 W. Zhou, X. Yu, Z. Zhang, X. Zou, H. Song and W. Zheng, *Int. J. Pharm.*, 2024, **650**, 123670.
20 X. Zhang, B. H. Tan and Z. Li, *Mater. Sci. Eng., C*, 2018, **92**, 1061–1074.
21 G. I. Peterson, A. V. Dobrynin and M. L. Becker, *Adv. Healthcare Mater.*, 2017, **6**, 1700694.
22 M. R. Pfau, K. G. McKinzey, A. A. Roth and M. A. Grunlan, *Biomacromolecules*, 2020, **21**, 2493–2501.
23 O. Uto, Y. Matsushita and M. Ebara, *Polym. Chem.*, 2023, **14**, 1478–1487.
24 M. Naddeo, A. Sorrentino and D. Pappalardo, *Polymers*, 2021, **13**, 627.
25 N. Mulchandani, K. Masutani, S. Kumar, H. Yamane, S. Sakurai, Y. Kimura and V. Katiyar, *Polym. Chem.*, 2021, **12**, 3806–3824.
26 B. G. Molina, G. Ocón, F. M. Silva, J. I. Iribarren, E. Armelin and C. Alemán, *Eur. Polym. J.*, 2023, **196**, 112230.
27 S. Ma, Z. Jiang, M. Wang, L. Zhang, Y. Liang, Z. Zhang, L. Ren and R. Ren, *Bio-Des. Manuf.*, 2021, **4**, 867–878.
28 M. M. Pérez-Madrigal, J. E. Shaw, M. C. Arno, J. A. Hoyland, S. M. Richardson and A. P. Dove, *Biomater. Sci.*, 2020, **8**, 405–412.
29 V. Castrejón-Comas, N. Mataró, L. Resina, D. Zanuy, A. Nuñez-Aulina, J. Sánchez-Morán, H. Enshaei, M. Arnau, H. Muñoz-Galán, J. C. Worch, A. P. Dove, C. Alemán and M. M. Pérez-Madrigal, *Carbohydr. Polym.*, 2025, **348**, 122941.
30 L. J. Macdougall, M. M. Pérez-Madrigal, M. C. Arno and A. P. Dove, *Biomacromolecules*, 2018, **19**, 1378–1388.
31 P. F. Finotti, L. C. Costa, T. S. Capote, R. M. Scarel-Caminaga and M. A. Chinelatto, *J. Mech. Behav. Biomed. Mater.*, 2017, **68**, 155–162.
32 M. J. Frisch, *et al.*, *Gaussian 16, Revision C.01*, Gaussian, Inc., Wallingford CT, 2016.
33 A. D. Becke, *J. Chem. Phys.*, 1993, **98**, 5648–5652.
34 C. Lee, W. Yang and R. G. Parr, *Phys. Rev. B: Condens. Matter Mater. Phys.*, 1988, **37**, 785–789.
35 S. H. Vosko, L. Wilk and M. Nusair, *Can. J. Phys.*, 1980, **58**, 1200–1211.
36 S. Miertus, E. Scrocco and J. Tomasi, *Chem. Phys.*, 1981, **55**, 117–129.
37 S. Miertus and J. Tomasi, *Chem. Phys.*, 1982, **65**, 239–245.
38 J. M. Ferri, O. Fenollar, A. Jorda-Vilaplana, D. García-Sanoguera and R. Balart, *Polym. Int.*, 2016, **65**, 453–463.
39 A. Fontana-Escartín, S. Lanzalaco, M. M. Pérez-Madrigal, O. Bertran and C. Alemán, *Plasma Processes Polym.*, 2022, **19**, e2200101.
40 A. Baranowska-Korczyc, A. Warowicka, M. Jasiurkowska-Delaporte, B. Grzeskowiak, M. Jarek, B. M. Maciejewska, J. Jurga-Stopac and S. Jurgaab, *RSC Adv.*, 2016, **6**, 19647–19656.
41 K.-M. Shin, T. Dong, Y. He and Y. Inoue, *J. Polym. Sci., Part B: Polym. Phys.*, 2005, **43**, 1433–1440.
42 K. Wasanasuk, K. Tashiro, M. Hanesaka, T. Ohhara, K. Kurihara, R. Kuroki, T. Tamada, T. Ozeki and T. Kanamoto, *Macromolecules*, 2011, **44**, 6441–6452.
43 D. Wu, D. Lin, J. Zhang, W. Zhou, M. Zhang, Y. Zhang, D. Wang and B. Lin, *Macromol. Chem. Phys.*, 2011, **212**, 613–626.
44 J. Kerns, H. Piponov, C. Helder, F. Amirouche, G. Solitro and M. Gonzalez, *Anat. Rec.*, 2019, **302**, 2030–2039.
45 A.-M. Vasi, M. I. Popa, M. Butnaru, G. Dodi and L. Verestiuc, *Mater. Sci. Eng., C*, 2014, **38**, 177–185.
46 D. Zanuy and C. Alemán, *J. Phys. Chem. B*, 2008, **112**, 3222–3230.
47 A. D. Boese, *ChemPhysChem*, 2015, **16**, 978–985.
48 M. M. Pérez-Madrigal, J. E. Shaw, M. C. Arno, J. A. Hoyland, S. Richardson and A. P. Dove, *Biomater. Sci.*, 2020, **8**, 405–412.
49 L. P. Modolo, W. R. França, M. M. O. Simbara, S. M. Malmonge and A. R. Santos, *Int. J. Polym. Anal. Charact.*, 2022, **28**, 73–87.
50 J. C. Rosa, J. J. Bonvent and A. R. Santos, *J. Biomater. Appl.*, 2022, **36**, 1641–1651.
51 V. A. da Silva, B. C. Bobotis, F. F. Correia, T. H. Lima-Vasconcellos, G. M. D. Chiarantin, L. De La Vega, C. B. Lombello, S. M. Willerth, S. M. Malmonge, V. Paschon and A. H. Kihara, *Int. J. Mol. Sci.*, 2023, **24**, 13642.
52 K. M. Z. Hossain, C. Zhu, R. M. Felfel, N. Sharmin and I. Ahmed, *J. Funct. Biomater.*, 2015, **6**, 564–584.
53 V. D. Dedeepiya, J. B. William, J. K. B. C. Parthiban, H. Yoshioka, Y. Mori, S. Kuroda, M. Iwasaki, S. Preethy and S. J. K. Abraham, *J. Spinal Surg.*, 2014, **1**, 16–24.
54 L. Fu, C. Ruan, C. Chen, Y. Gao, X. Bao, B. Liu, J. Zhou and W. Li, *J. Kunming Med. Univ.*, 2024, **45**, 7–14.
55 X. Mao, T. Li, J. Cheng, M. Tao, Z. Li, Y. Ma, R. Javed, J. Bao, F. Liang, W. Guo, X. Tian, J. Fan, T. Yu and Q. Ao, *Front. Bioeng. Biotechnol.*, 2023, **11**, 1103435.
56 A. Mobasseri, A. Faroni, B. M. Minogue, S. Downes, G. Terenghi and A. J. Reid, *Tissue Eng., Part A*, 2015, **21**, 1152–1162.